Benoît Beausir
Laboratoire de Physique et Mécanique des Matériaux,
Université de Metz,
Ile du Saulcy,
57045 Metz, France
Faculté de Génie,
Université de Sherbrooke,
Sherbrooke, QC, J1K 2R1, Canada

László S. Tóth
Laboratoire de Physique et Mécanique des Matériaux,
Université de Metz,
Ile du Saulcy,
57045 Metz, France

Fathallah Qods
Department of Material Science and Engineering,
School of Engineering,
Semnan University,
3519645399 Semnan, Iran

Kenneth W. Neale
Faculté de Génie,
Université de Sherbrooke,
Sherbrooke, QC, J1K 2R1, Canada

Texture and Mechanical Behavior of Magnesium During Free-End Torsion

Torsion experiments were carried out on pure magnesium (99.9%) and the magnesium alloy AZ71 under free-end conditions of testing. The alloy had an axisymmetric initial texture, while the pure Mg samples were prepared from a rolled plate with a nonaxisymmetric initial texture. The torque as a function of the twist angle was measured at different temperatures (room temperature, 150°C, and 250°C). During twisting, systematic shortening of the samples was observed (Swift effect). The evolution of the crystallographic texture was analyzed by electron backscattering diffraction measurements. The occurrence of dynamic recrystallization (DRX) was detected in pure Mg at 250°C. The Swift effect in the axisymmetric samples was simulated with the "equilibrium equation" approach using polycrystal modeling. In the nonaxisymmetric samples, the texture was simulated at different angular positions with the help of the viscoplastic self-consistent model. The changes in the textures due to DRX were explained in terms of the Taylor factor. Finally, the texture evolution was interpreted with the help of the behavior of ideal orientations and persistence characteristics of hexagonal crystals in simple shear.
[DOI: 10.1115/1.3030973]

Keywords: torsion, magnesium, texture, Swift effect

1 Introduction

Recent interest in using magnesium for automotive, aeronautical, and aerospace parts and other lightweight structures is due to its low density and reasonable mechanical properties. Nevertheless, the practical use of this material requires shape forming. During forming, large plastic deformations are applied to the material; thus, it is of primary importance to know its behavior under large deformations. There is, however, very scarce information about the mechanical behavior of Mg at large strains in torsion [1,2], as most of the testing is done in tensile loading where uniform deformation is limited due to strain localization.

In torsion testing it is possible to achieve very large uniform deformations without rupture or localization. Therefore, this test is convenient to determine the work hardening characteristics of metals. When the test is carried out under free-end conditions, an axial elongation or contraction—called the Swift effect [3]—can take place. In fixed-end testing, axial tensile or compression stresses accompany the shear strain. These axial effects are important phenomena in the validation of theoretical models [4]. Several works are available in the literature on texture development in torsion of metals on solid bars and tubes (for example, for cubic [5–10] and for hexagonal metals [1,2,11,12]).

The torsion test is most conveniently carried out on a full bar with a circular section. The angle of torsion and the torque are measured. These quantities must be converted into shear deformation and shear stress, respectively. Given that the deformation is inhomogeneous throughout the section of a full bar, it is necessary to carry out a certain analysis in order to obtain the shear stress. Owing to the fact that a radial material line remains radial during torsion, it is possible to use the Fields and Backofen formula [13] to obtain the "stress-strain" data from the "torque–twist angle" curve.

The analytical and experimental examinations of the behavior of polycrystalline metals subjected to very large deformations have been the subject of many studies. The development of deformation textures has also attracted considerable interest, mainly because this phenomenon leads to anisotropic properties, significant in many forming processes (e.g., stamping, extrusion, rolling, and wiredrawing). An understanding of the macroscopic stress and deformation responses of the polycrystals is particularly important in the numerical modeling of these metal forming operations [10].

In the present work, torsion test results are presented for the free-end torsion of pure magnesium and a magnesium alloy. The torque as a function of twist angle and the axial strain were measured at different temperatures. The stress-strain curves were obtained from the torque–angle of twist curves. Employing the approach based on the equilibrium equation [14,15], the evolution of the texture and the Swift effect were reproduced successfully using viscoplastic polycrystal modeling. The initial textures between the Mg alloy and pure Mg were very different; contrary to the Mg alloy, the initial texture of pure Mg is nonaxisymmetric with respect to its longitudinal axis. This was caused by the origin of the sample as it was cut out from a previously rolled plate and because rolling induces strong basal textures in Mg (see, for example, Ref. [16]). This characteristic of the initial texture generates heterogeneities of the texture in the sample during shear deformation. Dynamic recrystallization (DRX) also changed the texture in pure Mg at 250°C, which was interpreted with the help of the Taylor factor. Finally, an analysis of the texture evolution was carried out for these different cases with the help of the ideal orientations and persistence characteristics of hexagonal simple shear textures [17].

Contributed by the Materials Division of ASME for publication in the JOURNAL OF ENGINEERING MATERIALS AND TECHNOLOGY. Manuscript received January 7, 2008; final manuscript received October 10, 2008; published online December 22, 2008. Review conducted by Hamid Garmestani.

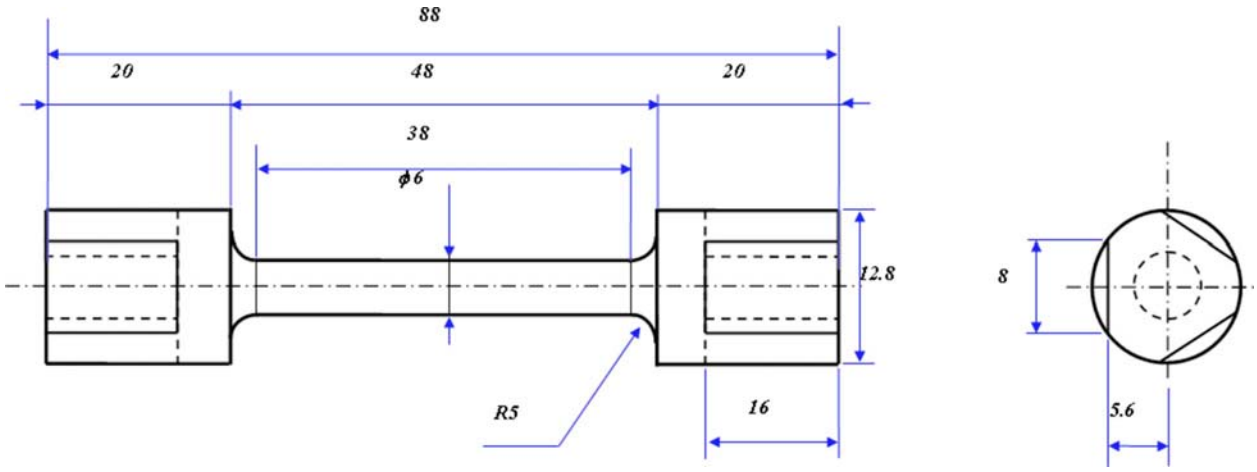

Fig. 1 Sample dimensions

2 Experiments

Free-end torsion tests were carried out on solid bars of pure magnesium (99.9%) and on the AZ71 Mg alloy (composition: 7 wt % Al, 1 wt % Zn, balance Mg). AZ71 was tested at three different temperatures (room temperature, 150°C, and 250°C) at a strain rate of 2×10^{-3} s^{-1}. The average initial grain size was about 40 μm in AZ71. Pure magnesium had an average grain size of 20 μm; it was tested at 250°C and at room temperature at two different strain rates: 7.7×10^{-4} s^{-1} and 7.7×10^{-3} s^{-1}. The testing at 250°C was conducted according to the following schedule: First the sample was positioned in the equipment, then it was heated slowly up to 250°C. After testing, the samples were cooled rapidly with water. The pure Mg samples had been cut from a rolled plate so that the longitudinal axis was parallel to the rolling direction (RD), while the AZ71 samples had been obtained from extruded materials. The sample dimensions are shown in Fig. 1. The samples were fixed to the grips with the help of three screws at each end. The torsion tests were carried out on a specially designed computer controlled apparatus with axial freedom of motion in a vertical setup. Due to the axial bearing, the samples were subjected to a constant axial loading of about 10 N (the weight of the bearing system). However, this load represented an axial stress of only about 0.35 MPa, which is practically negligible with respect to the flow stress of the material. All friction forces were also negligibly small with respect to the measured torque. The torque as a function of the twist angle, as well as the axial strain, was measured during the free-end torsion testing. These data were converted into shear stress–shear strain quantities using the Fields and Backofen formula [13]. This formula is more general than the Nadai formula [18] as it takes into account the strain rate sensitivity of the material response,

$$\tau_a = \frac{T}{2\pi a^3}\left[3 + \frac{d\ln T}{d\ln\theta} + \frac{d\ln T}{d\ln\dot{\theta}}\right] \tag{1}$$

Here τ_a is the shear flow stress at the outer radius (a) of the bar, T is the torque, and θ is the twist angle. The shear strain is calculated from the angle of rotation and refers always to the outer radius of the sample in this work.

The textures, before and after deformation, were measured by electron backscattering diffraction (EBSD) in a scanning electron microscope with a 1.0 μm resolution. Data acquisition and analyses were performed using the HKL software. For the texture measurements and for the metallographic study, the magnesium alloy samples were first polished mechanically then in an electrolyte that was composed of 85% phosphoric acid H_3PO_4 and 95% ethanol in a 3:5 proportion. In the EBSD measurements, the indexation quality was 80% in the nondeformed sample, while it was 40% in the deformed samples. This might appear to be a low indexation result; however, each grain was resolved by about the same quality of indexation. Moreover, further X-ray measurements have quantitatively confirmed the EBSD measurements. The pure magnesium sample was first mechanically polished then ion bombarded to finally obtain an indexation quality of about 75%.

3 Experimental Results

3.1 Sample Geometry of Torsion Deformed Pure Mg Bar. While the bar of the Mg alloy remained circular during torsion, the pure Mg bar showed a nonaxisymmetric deformation. Figure 2 displays photos of the pure Mg sample deformed at 250°C, showing the sample surface (Fig. 2(a)), a section parallel to the longitudinal axis (Fig. 2(b)), and one perpendicular to the z axis (Fig. 2(c)). Two helices developed on the surface of the bar, which are well visible in Fig. 2(a). Both of them appear to be split into two parallel helices. The places where the helices pass are called "ears," while the regions between them are called "faces" in this paper. The ear and face locations are actually positions with relatively large and small radii. Nonetheless, they were not always exactly at the maximum/minimum radii positions, just close to them. At a given cross section, perpendicular to the sample axis, there are two ears and two faces. Because of this, the sample cross section shows significant deviations from the initial circular shape (Fig. 2(c)).

3.2 Swift Effect. The shear deformation was very limited at room temperature testing, reaching only $\gamma\approx0.2$ in the alloy and about 0.4 in the pure metal. At 250°C, the maximum plastic shear strain was much larger; for the pure Mg it was about 1.7. The experimental results for the length changes are presented in Fig. 3. In all tests, there is shortening for all conditions of temperature or strain rates. This shortening could reach 1.8% for AZ71 and 9% for pure magnesium. (The initial transient displaying lengthening is within the error of the measurement.) It can be noted that shortening stops in pure magnesium, while AZ71 shortens steadily.

3.3 Strain Hardening. Figure 4 shows the strain hardening curves for the AZ71 alloy derived from the experimental measurements of the torque–twist angle by using Eq. (1). Concerning the pure Mg samples, as they had no axisymmetric textures, Eq. (1) could not be applied to them because rotational isotropy around the bar axis is assumed in the Fields and Backofen formula. As can be seen, the yield stress decreases a little between 20°C and 150°C, while a strong decrease occurs between 150°C and 250°C. It indicates that there is a change in the deformation mechanism, which is probably the occurrence of deformation

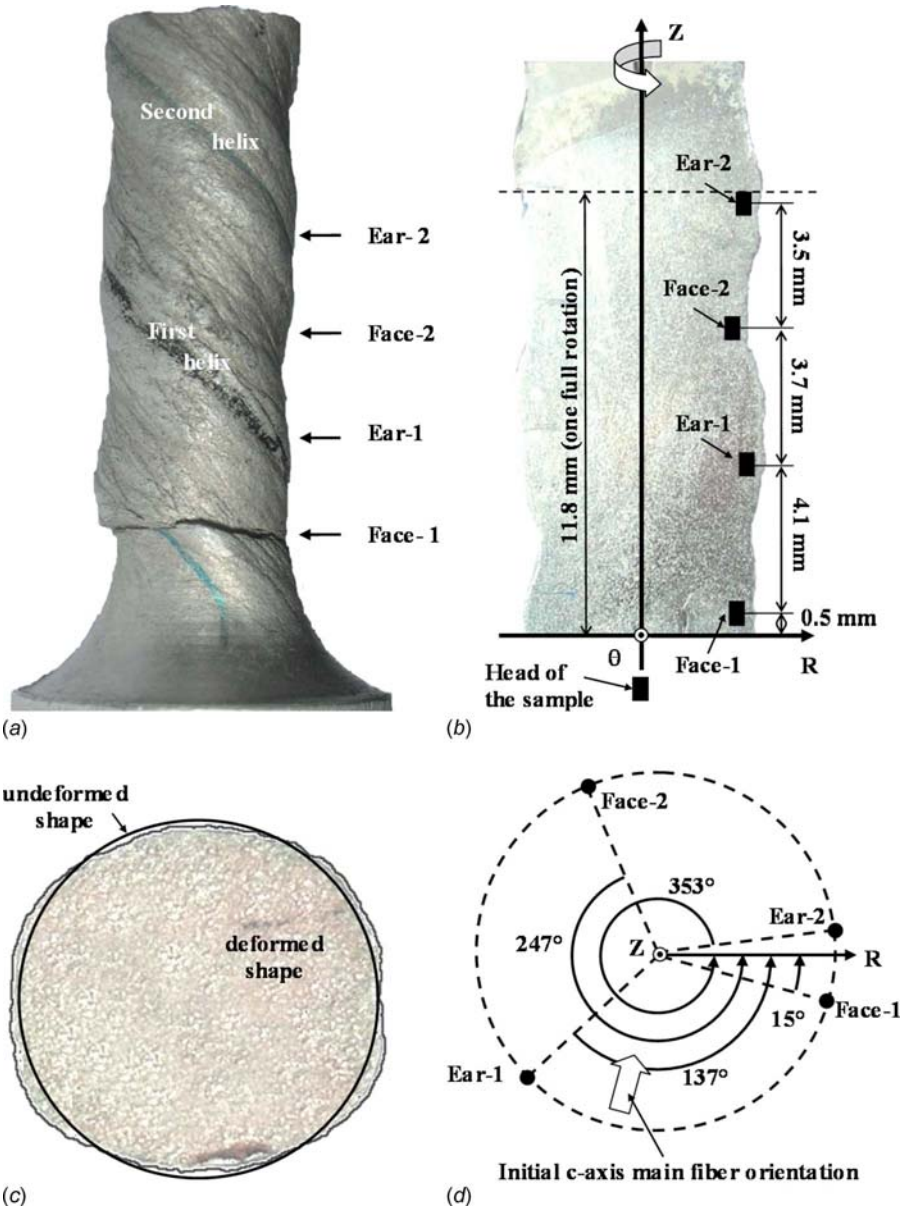

Fig. 2 Shape of pure Mg sample deformed at 250°C with a strain rate of 7.7×10^{-4} s^{-1}. (*a*) Photo of the surface of the bar after torsion displaying the helices. (*b*) Longitudinal cross section of the deformed specimen with black spots showing the positions where textures were measured. (*c*) Cross section of the deformed specimen showing its elliptical shape. (*d*) Positions of the measurement places before deformation as indicated by the black full circles. The angles are the rotations that took place to reach the final positions.

twinning, which is virtually inactive at 250°C. While twinning is very active at room temperature [19], it has been observed in Barnett et al. [20] that twinning is strongly reduced at high homologous temperatures. There is also an important difference in the rate of strain hardening between 150°C and 250°C. It is much higher at 150°C, an effect that can also be attributed to twinning, which is still active at this temperature.

3.4 Textures and Microstructures. The grain structure after deformation at 250°C is shown in Fig. 5(*a*) for the AZ71 and in Fig. 5(*b*) for pure Mg. As can be seen, the large axes of the grains are inclined at an angle of about 30 ° with respect to the longitudinal axis in the shear direction for the AZ71 sample at a shear of 0.9 near the outer surface of the sample. (The same inclination angle is obtained from a visual analysis and using the HKL software of the EBSD equipment.) From the applied shear, nearly the same angle can be obtained for the inclination of the main grain axis starting from a spherically shaped grain under simple shear [21],

$$\alpha = \frac{1}{2}\arctan\frac{2}{\gamma} = 32.9\ ^\circ \tag{2}$$

This agreement of the angles suggests that there was no dynamic recrystallization in the AZ71 material during torsion at 250°C. However, the equiaxed grain structure in pure Mg after a shear of 1.6 implies that dynamic recrystallization took place in this material at 250°C (Fig. 5(*b*)).

The color codes of the grains in Fig. 5 indicate that the orientation distribution is not random in the AZ71 and pure Mg

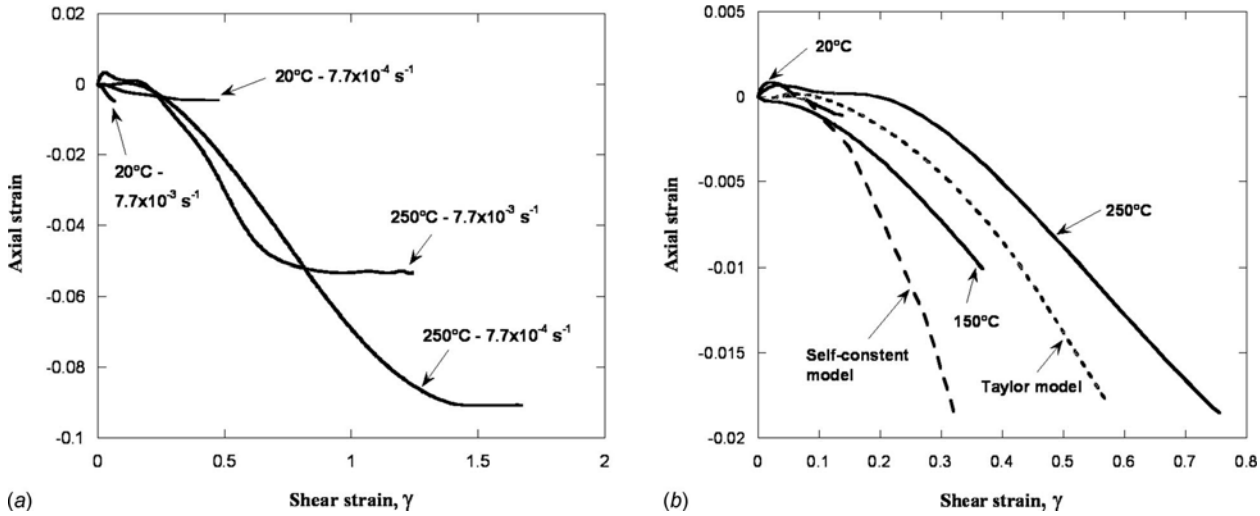

Fig. 3 Shear strain–axial strain curves for (*a*) pure magnesium and (*b*) AZ71

samples; there must be significant textures in both materials. Precise information about the textures was obtained with EBSD measurements; they are shown in Fig. 6 for the AZ71 sample and in Figs. 7 and 8 for pure Mg. In all pole figures shown in this paper, the projection plane is the plane with normal r (the radial axis), the shear direction is horizontal (θ axis), and the axial direction (z) is vertical. Figure 9 displays the ideal fiber orientations of hexagonal crystals for simple shear [17].

The texture in the deformed AZ71 sample in Fig. 6 was measured within a 500×650 μm^2 surface parallel to the longitudinal axis of the sample. The initial experimental texture is presented in Fig. 6(*a*). As can be seen, the initial texture is a $\langle 10\bar{1}0 \rangle \| z$ fiber texture with moderate strength. That is, the c axis is mostly perpendicular to the axis of the bar; it lies in the shear plane during torsion. Figure 6(*b*) shows the texture in a zone where the average shear deformation was 0.9. After a shear of $\gamma = 0.9$, the texture is just slightly stronger but is very different from the initial texture. It seems to be rotated by an angle of about 30 ° around the radial axis with respect to the initial texture.

The initial texture in pure Mg is shown in Fig. 7, while the deformation textures (after a shear strain of 1.6 at the outer surface and at a rate of shear 7.7×10^{-4} s^{-1} at 250 °C) are displayed in Fig. 8. Due to the origin of the Mg sample (from a rolled plate, cut out parallel to the RD), the initial texture of the pure Mg samples was not axisymmetric: a $\langle 0002 \rangle \| \mathrm{ND}$ fiber was identified (ND: normal direction to the rolled plate). This ND direction, which is the fiber axis, is identified in Fig. 2(*d*) with a large white arrow. Again, the c axis lies in the plane of the shear (perpendicular to the z axis), similar to the AZ71 material. However, it is now oriented only in one specific direction, the ND of the plate from which the sample originated, and this is the fiber axis.

The deformation textures were examined at four locations situated at a distance of 500 μm from the external surface. These locations are identified in Figs. 2(*a*) and 2(*b*); they are named Ear-1, Ear-2, Face-1, and Face-2. They were measured in the same vertical section; however, their initial position is also important with respect to the initial texture because it was not axisymmetric. This is why the initial positions of the measurement places are shown in Fig. 2(*d*) together with the corresponding rotations around the z axis that took place during the twisting. These rotations will be used in the simulation of the textures (see below). The textures that correspond to these initial positions are plotted in the first column of Fig. 8; they are simply the initial textures rotated by the angles shown in Fig. 2(*d*). These textures were sheared with the same positive shear and gave the final measured textures that were measured at the places indicated in Fig. 2(*b*); they are plotted in the second column in Fig. 8. These textures are quite different from each other. (Please note that they would be identical if the initial texture of the bar was axisymmetric.) All deformation textures seem to be mainly a rotated version of the corresponding initial textures around the local radial R axis.

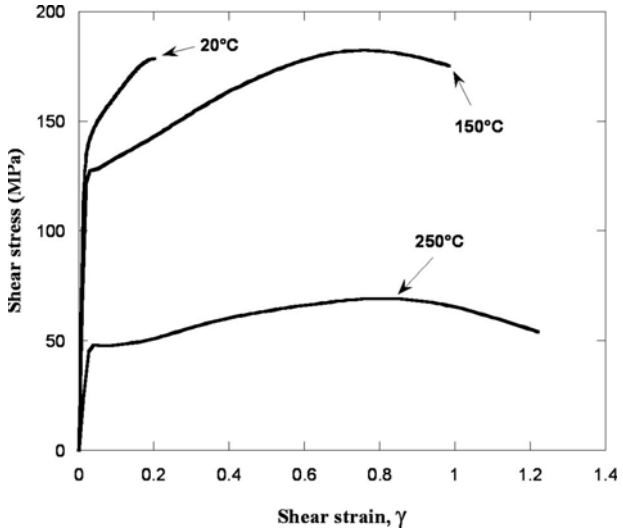

Fig. 4 Stress-strain curve for AZ71 obtained in free-end torsion at a shear rate of 2×10^{-3} s^{-1}

4 Polycrystal Simulations

For the modeling of the deformation textures and the Swift effect, the viscoplastic polycrystal self-consistent code developed by Lebensohn and Tomé [22] (VPSC, Version 7) was applied. The evolution of the grain shape with deformation was modeled, starting with initially spherical grains. For comparison purposes, the Taylor viscoplastic approach was also employed. The initial textures measured by EBSD were used as input grain orientations in the modeling. Several families of the slip systems are present in the hexagonal structured materials. They are basal $\{0001\}\langle 1\bar{2}10 \rangle$, prismatic $\{1\bar{1}00\}\langle 11\bar{2}0 \rangle$, pyramidal $\langle a \rangle$ $\{10\bar{1}1\}\langle \bar{1}2\bar{1}0 \rangle$, pyramidal $\langle c+a \rangle$ type-I $\{10\bar{1}1\}\langle 2\bar{1}\bar{1}\bar{3} \rangle$, and pyramidal $\langle c+a \rangle$ type-II $\{2\bar{1}\bar{1}2\} \times \langle \bar{2}113 \rangle$ (see Fig. 10). An important point in hexagonal crystal-

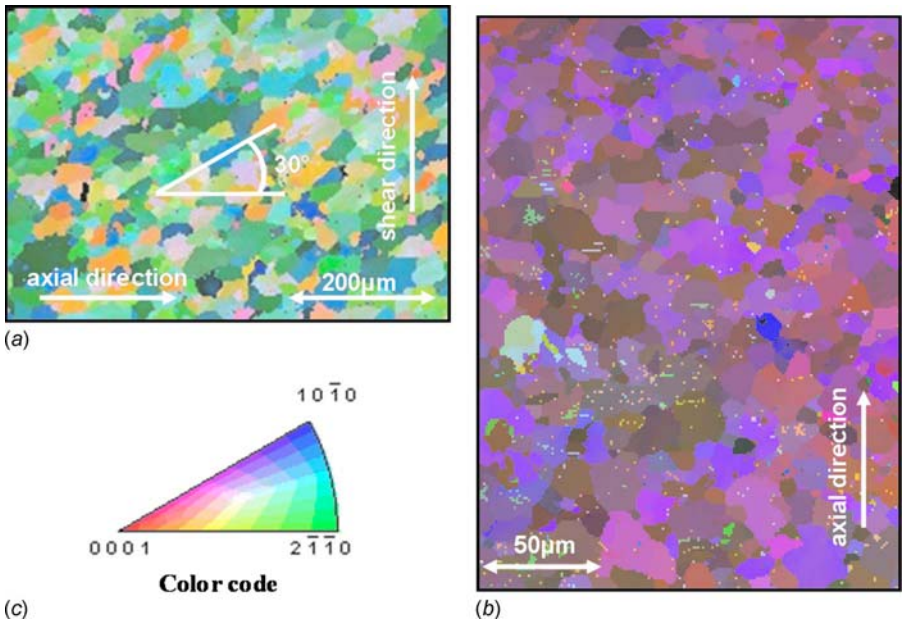

Fig. 5 EBSD maps after deformation of (*a*) 0.9 shear in AZ71 and (*b*) 1.6 shear in pure magnesium. The color code (*c*) corresponds to the direction of the *r* axis of the sample within the unit triangle of the hcp stereographic projection.

lography is that the gliding resistances of the various families of slip systems are different. In the present investigation, several sets of the reference shear stresses were considered for the simulation. The simulations that were selected were those that corresponded best to the experimental observations. In this way, it was found that the following set of reference stresses gave the best results for pure Mg [1,8,6], where these values refer to the slip systems in the following order: $\langle \tau_0^{\text{basal}}/\tau_0^{\text{basal}}, \tau_0^{\text{prism}}/\tau_0^{\text{basal}}, \tau_0^{\text{pyr}<a>}/\tau_0^{\text{basal}}, \tau_0^{\text{pyr}<c+a>-\text{I}}/\tau_0^{\text{basal}}, \tau_0^{\text{pyr}<c+a>-\text{II}}/\tau_0^{\text{basal}} \rangle$. The same set was employed by Agnew et al. for different Mg alloys [23]. However, for the AZ71 alloy, slightly different values were identified in the present work: (1,8,8,4.5,4.5). Deformation twinning was not considered for both materials in the simulations as only the high temperature case was examined (250°C). While twinning is an operational deformation mode at room temperature [24], its activity can be neglected at high homologous temperatures [20]. Concerning the strain rate sensitivity at 250°C, the value of $m=0.2$ was used for both pure Mg and AZ71 because experiments reported m-values in this range for different Mg alloys at high homologous temperatures ($m=0.15$ in Agnew and Duygulu [25] and $0.14 \leq m \leq 0.5$ in Kim et al. [26]). This m-value is considered to be the same as the strain rate sensitivity exponent of slip in the constitutive behavior [27],

$$\tau^{s,f} = \tau_0^f \operatorname{sgn}(\dot{\gamma}^{s,f}) \left| \frac{\dot{\gamma}^{s,f}}{\dot{\gamma}_0} \right|^m = \tau_0^f \frac{\dot{\gamma}^{s,f}}{\dot{\gamma}_0} \left| \frac{\dot{\gamma}^{s,f}}{\dot{\gamma}_0} \right|^{m-1} \tag{3}$$

Here $\tau^{s,f}$ is the resolved shear stress in the slip system indexed by s of the family indexed by f, $\dot{\gamma}^{s,f}$ is the slip rate, and the τ_0^f value is the reference stress level (at which the slip rate is $\dot{\gamma}_0$). The reference shear rate $\dot{\gamma}_0$ is supposed to be the same for all slip systems. Equation (3) has been widely used in crystal plasticity simulations [27–35]. The slip systems are grouped into "families" for which purpose the index f is used. It is assumed here that the reference shear stress τ_0^f is the same within a given slip system family but can be different from one family to another. Slip system hardening due to deformation was not modeled. The simulation results obtained for the AZ71 sample are presented in Figs. 6(*c*) and 6(*d*) at the experimental strain ($\gamma=0.9$) and also at a larger strain ($\gamma=4.0$) for a better understanding of the global movement of the grains. These results were obtained for simple shear; the relatively small Swift effect was neglected.

The simulation of the Swift effect was performed by using the approach based on the equilibrium equation (see the model in Refs. [14,15]) for the AZ71 alloy and only for 250°C. In this modeling, the bar is divided into five layers, and in each layer there are 691 grain orientations representing the initial texture. The modeling is only applicable to textures that are axisymmetric, so the Swift effect for the Mg samples was not modeled. Both the self-consistent and the Taylor model were applied. Work hardening was also neglected in these simulations; however, it will be shown in Sec. 5.1 that the strain hardening curve is faithfully reproduced at 250°C. The results of the simulations of the Swift effect are shown in Fig. 3(*b*), in comparison with the experiments. In agreement with the measurements, shortening was obtained in the modeling. The Taylor model, however, reproduces the experimental shortening better than the self-consistent model. The predicted textures when the Swift effect is accounted for are shown in Figs. 6(*e*) and 6(*f*) in the form of pole figures. Again, the Taylor model seems to better reproduce some features of the textures, such as the general rotation angle of the texture, which is overestimated by the self-consistent model.

For the modeling of the texture development in pure Mg, simple shear was assumed (i.e., the shortening was neglected). Thus, the imposed velocity gradient in the local Cartesian reference system corresponding to simple shear was the following:

$$\boldsymbol{L} = \begin{pmatrix} 0 & \dot{\gamma} & 0 \\ 0 & 0 & 0 \\ 0 & 0 & 0 \end{pmatrix}_{1,2,3} \tag{4}$$

where axis 2 is parallel to the z plane normal and axis 1 is the shear axis in the θ direction.

Simulations were performed at each location where the texture was measured up to a shear of 1.3, corresponding to the local shear, and the results are displayed in the third column of Fig. 8.

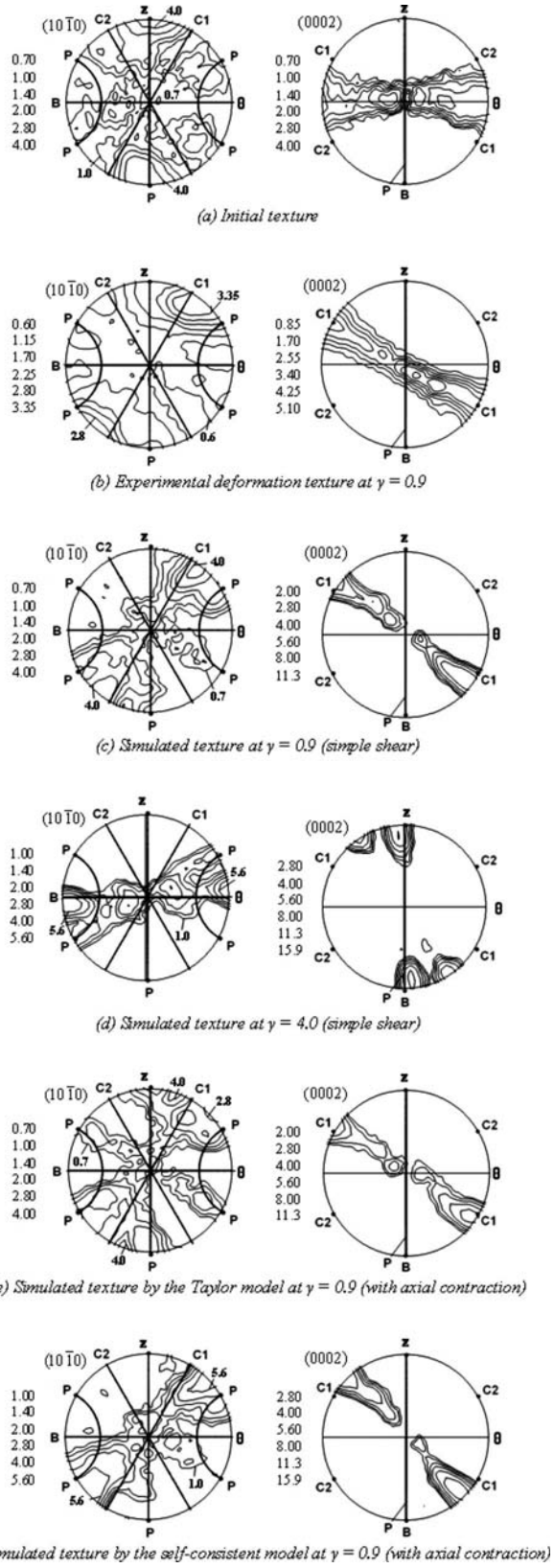

Fig. 6 Measured and simulated texture evolution during torsion of magnesium AZ71

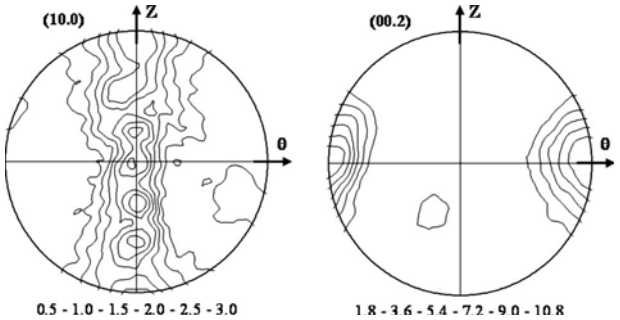

Fig. 7 Initial texture of the pure Mg sample, measured in the undeformed part, in the head of the sample. Note that this texture is strongly nonaxisymmetric. The initial plate normal direction is along the horizontal axis.

5 Discussion

With the help of the so-called persistence parameter P, the ideal orientations for hexagonal materials in simple shear were identified recently in Beausir et al. [17]. P is defined from the lattice spin $\underline{\underline{\Omega}}$ as follows:

$$P(\boldsymbol{g},\underline{\underline{\dot{\varepsilon}}}) = \ln\frac{1}{|\Omega(\boldsymbol{g},\underline{\underline{\dot{\varepsilon}}})|/\bar{\dot{\varepsilon}}} \tag{5}$$

where $\boldsymbol{g}$ denotes the orientation $\boldsymbol{g}=(\varphi_1,\varphi,\varphi_2)$, $\underline{\underline{\dot{\varepsilon}}}$ is the strain rate tensor, and $\bar{\dot{\varepsilon}}$ is the applied von Mises equivalent strain rate. The persistence parameter takes high values in regions of orientation space where the rotation rate of orientations is low. Making maps of P in orientation space, the ideal orientations—all of them are fibers—could be identified for the simple shear test and for hexagonal crystals. Five fibers were found (B, P, Y, C_1, and C_2), which were defined in orientation space with the Euler angles $(\varphi_1,\varphi,\varphi_2)$ that correspond to the reference system defined with the x_1 axis parallel to the shear direction (θ), x_2 being the shear plane normal (z axis), and x_3 being the radial axis (r). They are B (0 °,90 °,0–60 °), P (0 °,0–90 °,30 °), Y (0 °,30 °,0–60 °), C_1 (60 °,90 °,0–60 °), and C_2 (120 °,90 °,0–60 °). They correspond, respectively, to the basal, prismatic, pyramidal $\langle a\rangle$, pyramidal $\langle c+a\rangle$ type-I, and pyramidal $\langle c+a\rangle$ type-II families (see the slip system families in Fig. 10). According to Beausir et al. [17], the principal ideal fibers in magnesium are B and P; they are shown with thicker lines in Fig. 9. The persistence parameter itself is not sufficient to describe the behavior of the orientations. The rotation field in vector form is also necessary. They were also presented in Beausir et al. [17] and will be used in the present paper to explain the texture evolution in the AZ71 alloy and in pure magnesium during the torsion test.

5.1 Texture Evolution and Hardening in AZ71. The evolution of the texture during torsion can be understood with the help of the simulations that are displayed together with the experiments in Fig. 6. It can be seen that the simulated texture at the same shear strain as the experiment (γ=0.9) shows the texture rotated around the r axis. The predicted rotation angle is 35 °, while the experimental value is 30 °. It is interesting to note that this rotation angle is even larger than the rigid body rotation, which can be obtained from the shear of 0.9, which is only 26 °. It is apparent from the pole figure that a rotation of 90 ° in the direction of shear would be needed in order to reach the ideal B fiber. As the strain is relatively low (0.9), it is not enough to reach the ideal position, not even if the rotation rate is equal to the rigid body spin. That is, the initial fiber is very far from the ideal position; as its persistence is very low, it must rotate quickly. The simulation in Fig. 6(*d*) for the shear of 4.0 illustrates that it is possible to reach the B fiber if the strain is very large. This simulated texture shows an

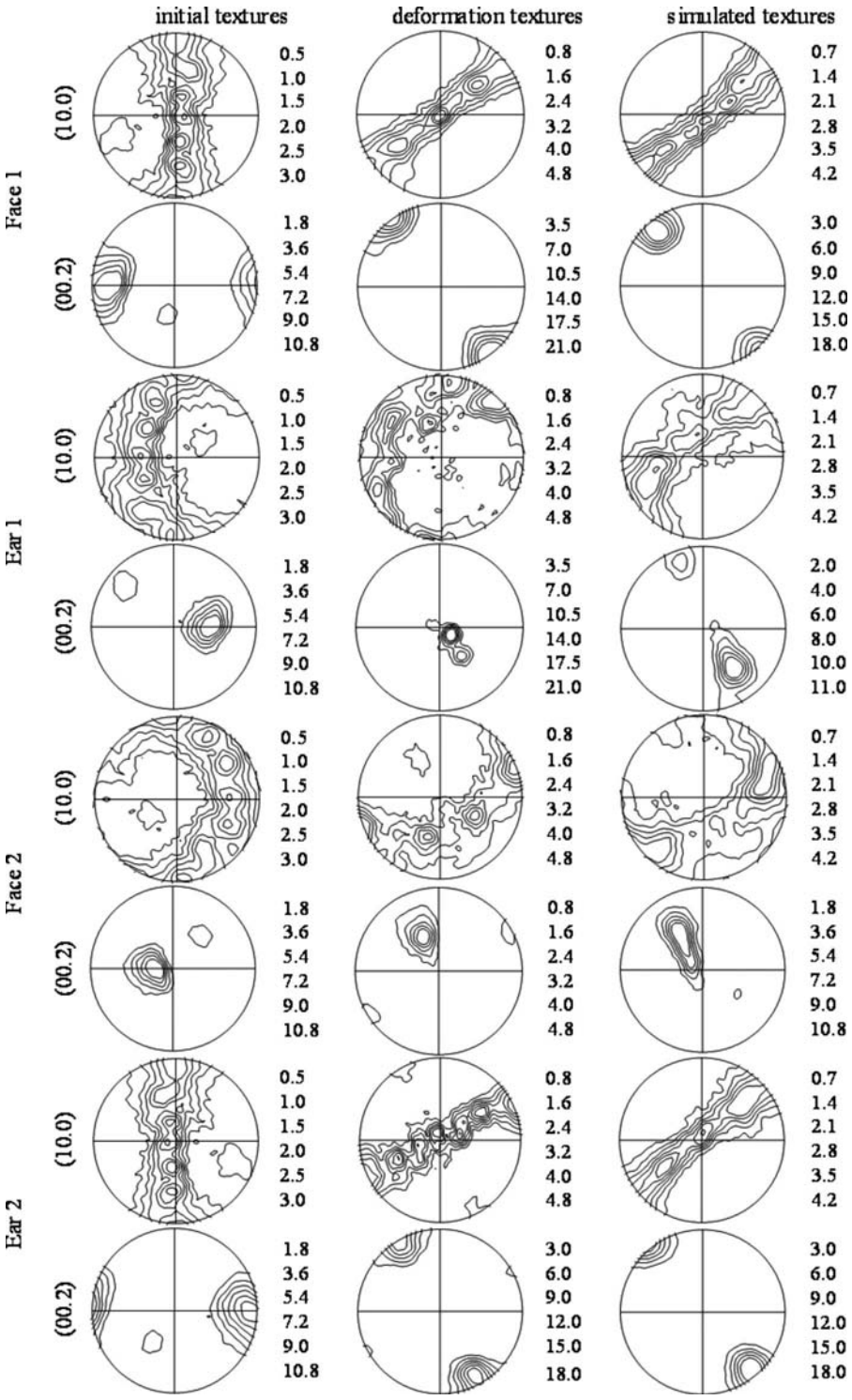

Fig. 8 Texture evolution in the four measured positions: Face1, Ear1, Face2, and Ear2 in (10.0) and (00.2) pole figures

interesting feature, namely, a certain split of the main component that is clearly visible in the (0002) pole figure. Such a split can also be observed in experiments as well as in simulations at large strains that can be attained in the Equal Channel Angular Extrusion (ECAE) of Mg (see Agnew et al. [23] and Beausir et al. [32]). It can be attributed to an effect of grain shape. Such a split does not happen in Taylor modeling. At $\gamma=4$, the grain shape is extremely elongated, which is accounted for in the so-called interaction equation of the self-consistent model, leading to the observed "split" nature of the main texture component. The geometrically predicted shape is a very elongated cigar at $\gamma=4$; nevertheless, grain subdivision happens during severe plastic deformation, which drastically reduces the ellipticity of the grains. When the grain shape is reset during self-consistent modeling, the split nature of the simulated texture is significantly reduced. Such simulation work was carried out by Beyerlein et al. [33] for ECAE of fcc polycrystals and is in development for the large strain torsion of Ni–Al [34].

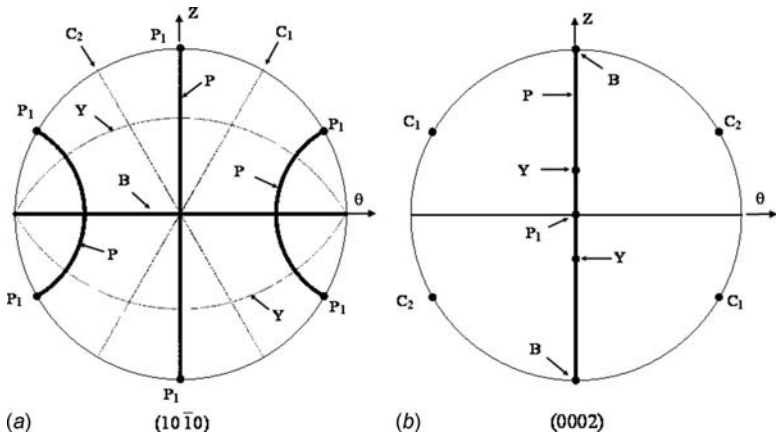

Fig. 9 Ideal orientations of magnesium under simple shear as they appear in the (*a*) (10.0) and (*b*) (00.2) pole figures (Beausir et al. [17]). The fiber names are B, basal; P, prismatic; Y, pyramidal; C_1, pyramidal-I; and C_2, pyramidal-II.

Figure 11 shows the textures in Orientation Distribution Function (ODF) format, in the $\varphi_2=0$ ° section of the orientation space. This is the section where the $\langle 10\bar{1}0\rangle \| z$ initial fiber is located, at the $\varphi_1=90$ ° position parallel to the φ axis of Euler space. The rotation field is also plotted together with the ODF in order to see the evolution of the texture. It is shown by the arrows that are obtained from the lattice spin $\dot{g}=(\dot{\varphi}_1,\dot{\varphi},\dot{\varphi}_2)$. The length of the rigid body spin vector is also indicated in Fig. 11(*a*). As can be seen, the main trend of the rotation is in the direction of the rigid body spin with a final destination to the B fiber. Nevertheless, by approaching the B fiber, the rotation field is not only a rotation parallel to the rigid body spin; there is a φ component, too. A close inspection of the lattice spin vectors reveals that the rotation spin around the r axis (the φ_1 component of the rotation vectors) depends on the φ position; it is maximum along the $\varphi_1=90$ ° line. At this location, in the initial position ($\varphi_1=90$ °, $\varphi=90$ °, $\varphi_2=0$ °), it is even twice as high as the rigid body spin. This peculiarity of the rotation in hexagonal crystals was shown in the Appendix of Beausir et al. [32]. This is the reason why the rotation of the texture (30 °) is larger than the rigid body rotation (26 °).

When the strain is very high (at $\gamma=4$), the texture is further rotated in the direction of the rigid body spin and approaches

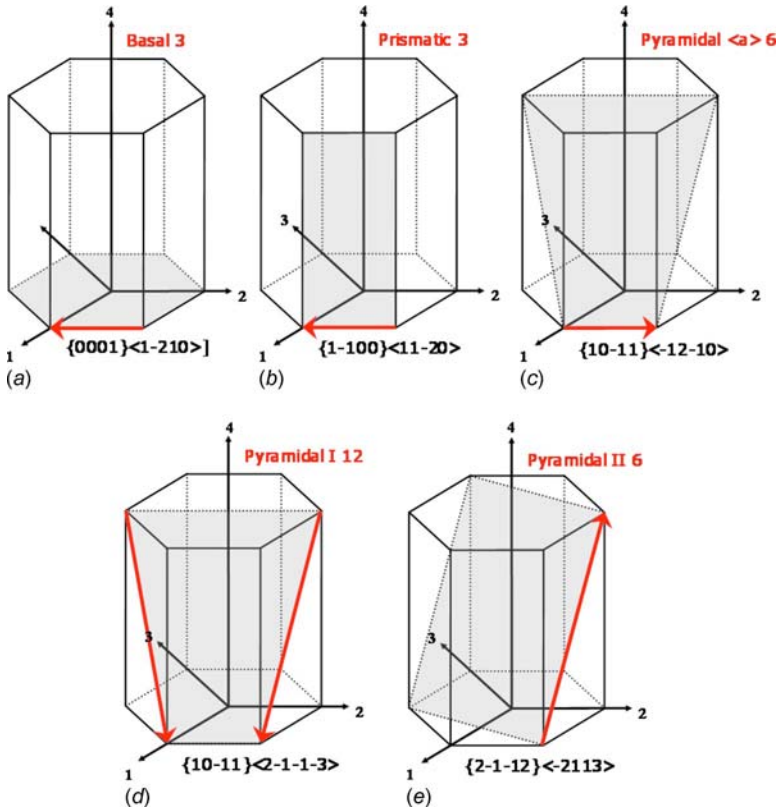

Fig. 10 Slip system families in hexagonal structures; basal, prismatic, pyramidal $\langle a\rangle$, pyramidal $\langle c+a\rangle$/I, and pyramidal $\langle c+a\rangle$/II

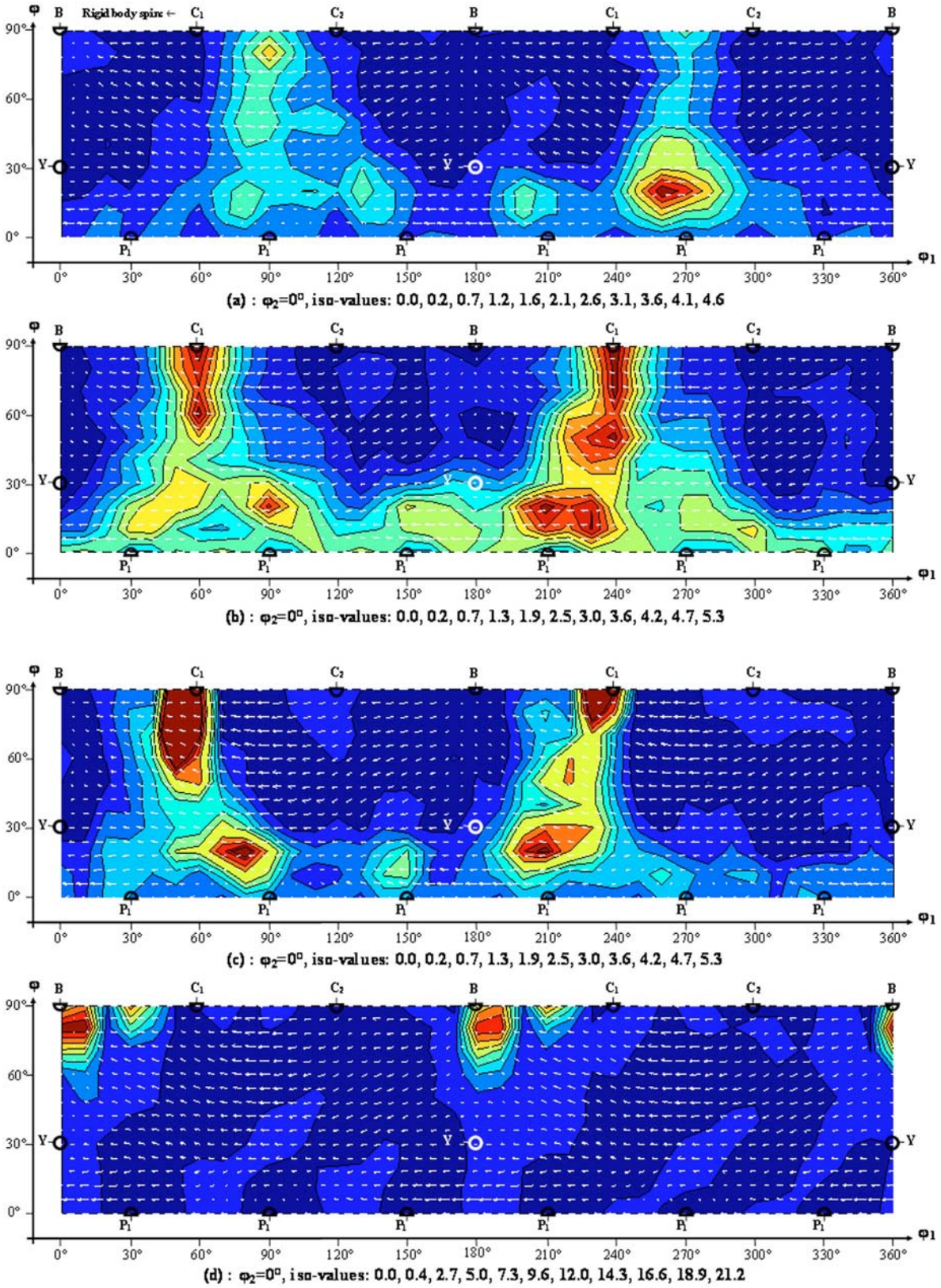

Fig. 11 Texture evolution for the torsion of AZ71 in the $\varphi 2 = 0^\circ$ ODF section. (*a*) Initial texture, (*b*) deformation texture, (*c*) simulated texture by simple shear at $\gamma = 0.9$, and (*d*) simulation by simple shear at $\gamma = 4.0$.

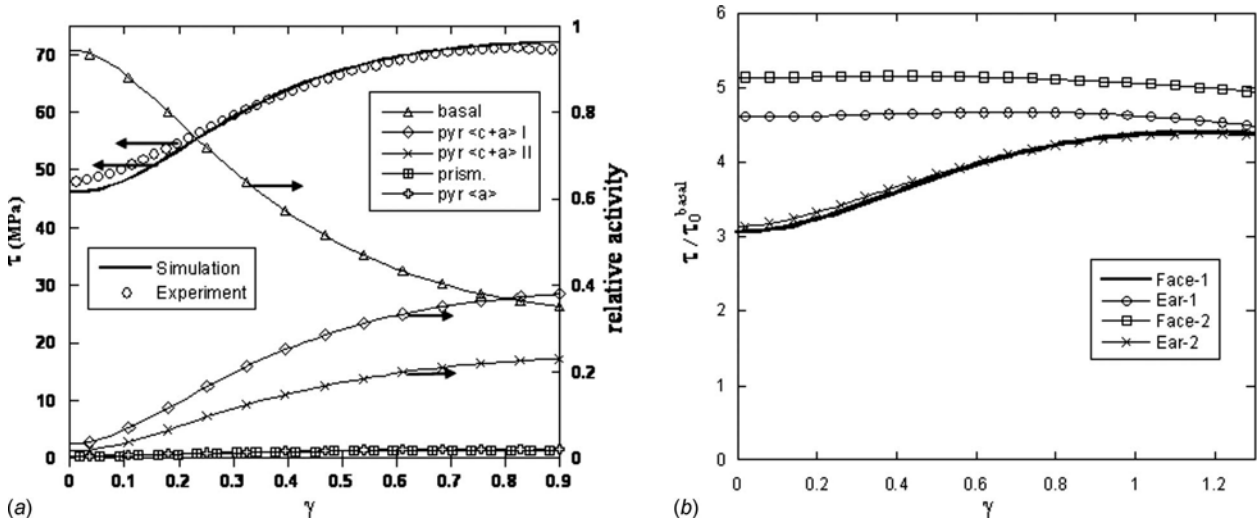

Fig. 12 (*a*) **Comparison of experimental and simulated strain hardening in AZ71.** (*b*) **Simulated strain hardening at the four measured positions in the pure Mg bar.**

more the ideal B fiber; see the simulation result in Fig. 11(*d*). There also appears a secondary peak, which is farther from the ideal position. This is the same as the one seen in the pole figure in Fig. 6(*d*) and discussed above.

Another effect in the development of the texture shown in Figs. 6(*d*) and 11(*d*) is that the main component only approaches the ideal position but does not reach it completely; there remains a "tilt" with respect to the ideal B fiber position. Such tilts are due to the convergent nature of the rotation field near the ideal positions, which are approached only from one side in orientation space [17].

Although hardening was neglected in the present simulations, appreciable hardening was observed in the simulated shear stress–shear strain curve of the AZ71 material (see Fig. 12(*a*)). Moreover, it agrees well with the experimental curve. To understand this phenomenon, the slip system activities are also plotted in Fig. 12(*a*). As can be seen, there are significant changes; basal slip decreases from an initial 93% to 35%, while the pyramidal systems become much more active. (Prismatic slip remains under 3% of activity.) Therefore, the observed apparent hardening is due to increased activity of the harder stress slip systems that become more active as a consequence of the orientation changes. This effect is called "textural hardening." A very similar effect was simulated in the work of Staroselsky and Anand [24]—also without hardening—in AZ31 and at room temperature where twinning had to be taken into account.

5.2 Swift Effect in AZ71. As shown in Fig. 3(*b*), both the Taylor and self-consistent models predict shortening. Nevertheless, it is quite unusual that the length changes predicted by the Taylor model approach better the measured values than the more sophisticated self-consistent model. At the same time, the texture predicted by the Taylor model is also better (see Fig. 6). The differences between the textures obtained by the self-consistent model for simple shear (Fig. 6(*c*)) and with axial strain included (Fig. 6(*f*)) are also significant. Of course, these differences can be entirely attributed to the axial strain, which is not very small in the self-consistent case; it is about 19% at a shear of 0.9, therefore largely overestimated.

These simulation results are good examples to show the sensitivity of the Swift effect to the modeling conditions. This is why this effect is particularly suitable to assess large strain polycrystal models. In the self-consistent model, it is the grain-shape effect that is the most important element of the modeling. Initially spherical grains were considered, which were assumed to interact with their surrounding in a homogenized way. Perhaps at these relatively low strains ($\gamma < 0.9$), the shape effect is overestimated in the self-consistent model, and this is the reason why the Taylor model works better. Nevertheless, at large strains, the self-consistent model always gives better results (see, for example, Ref. [35]). Further studies are needed to explore this shape effect in relation to the Swift effect; a detailed study is in preparation by Tomé et al. [34].

5.3 Texture Evolution in Pure Magnesium. The peculiarity of the pure Mg sample is that it does not have an axisymmetric texture. As the samples were cut from a rolled plate, they contain a texture that is not the same at different angular positions with respect to the local shear. Thus, at a given θ angle, the initial texture is rotated with respect to the local shear, as illustrated by the rotation angles in Fig. 2(*d*). This angle increases linearly with the z coordinate due to the torsion of the sample, at least in uniform torsion—which is not perfectly valid in our case—but will be used as an approximation to calculate the rotation angles. Thus, the value of the rotation angle of a given position due to the applied shear was obtained from the following relation:

$$\theta(z) = \frac{\gamma \cdot z}{r} \tag{6}$$

Here γ and r are the shear strain and the radial position, respectively. A rotation of 360 ° (i.e., when the texture is again the same) belongs to a displacement of $\Delta z = 11.78$ mm in the vertical direction along the specimen (see Fig. 2(*b*)).

In order to simulate the evolution of the texture at the measured positions, simple shear was applied as defined in Eq. (4). The initial texture was first positioned with respect to the reference system using the rotation angles shown in Fig. 2(*d*). Then, positive simple shear was applied with a shear value of 1.3 with the VPSC model (this value of shear corresponds to the shear at the measurement locations of the textures). As can be seen in Fig. 8, the simulations performed with the VPSC model reproduce the experimental measurements with a good agreement in positions Face-1, Face-2, and Ear-2. The agreement is less satisfactory in the Ear-1 position, but the general trend is reproduced.

5.3.1 Texture in the Face-1 Position. The initial texture for the Face-1 position is presented also in ODF format in Fig. 13(*a*) in the $\varphi = 90$ ° ODF section. As can be seen, the initial fiber is located at the $\varphi_1 = 90$ ° position. After the applied shear $\gamma = 1.3$, the fiber is displaced to the left by about 50 ° by a rotation around the r axis, also visible in the pole figures in Fig. 8. The velocity field

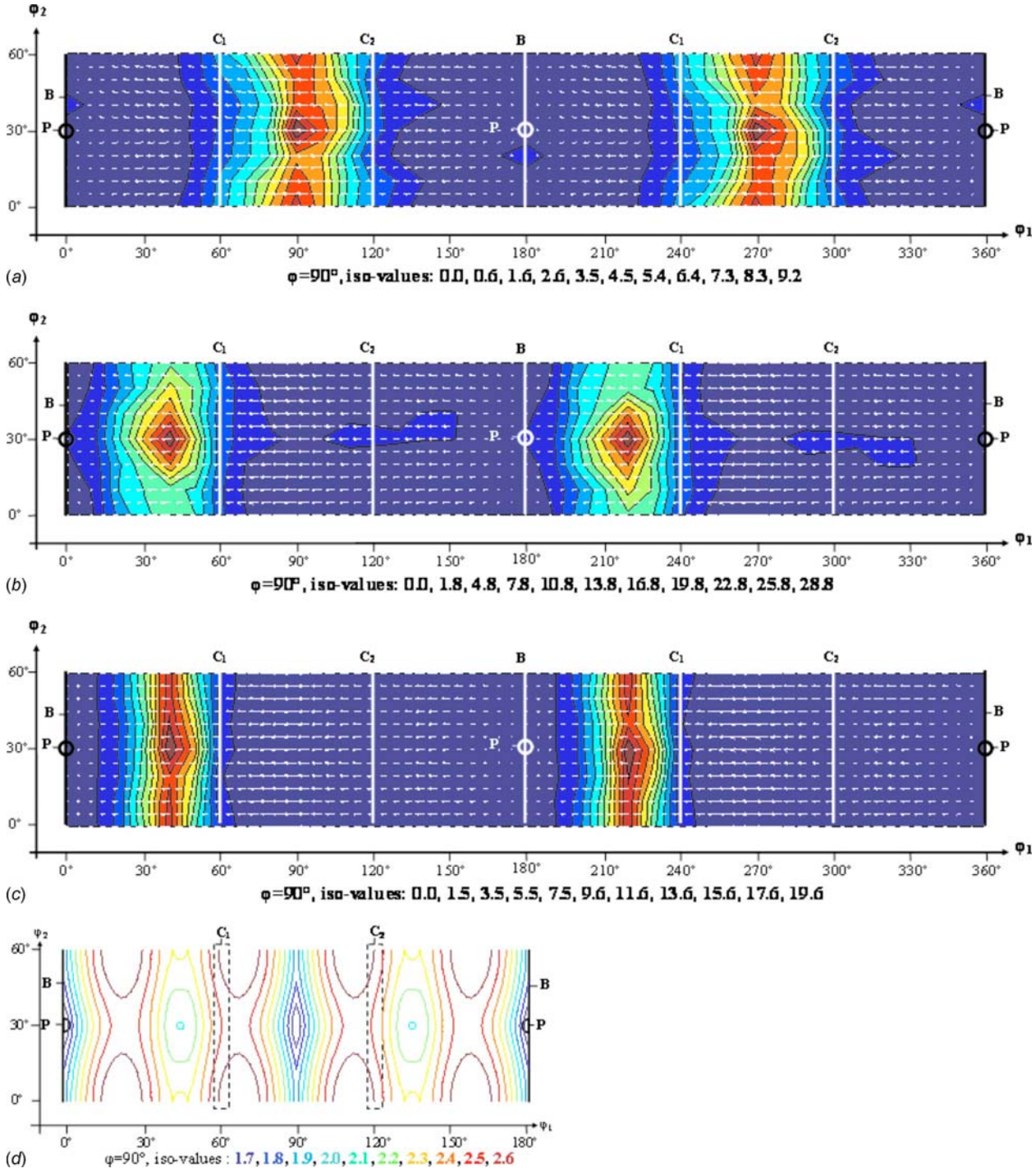

Fig. 13 Texture evolution for torsion of pure Mg in the ⟨⟨Face-1⟩⟩ position in the $\varphi=90$ ° ODF section. (*a*) Initial texture, (*b*) deformation texture, (*c*) simulated texture, and (*d*) map of the Taylor factor in the same section of the orientation space.

associated with a positive simple shear applied on a magnesium crystal is superposed in the ODF figures. It shows a clear displacement in the decreasing φ_1 direction, which is also the direction of the rigid body rotation. However, this value of rotation is unusually high. Just like in the AZ71 material, it is again more than the applied rigid body rotation, which is only 37 ° for a shear of $\gamma=1.3$. So this peculiarity has the same explanation, which was forwarded above for the AZ71 material; the fiber texture is very far from the ideal B fiber position, so it rotates very fast. It can be seen from the initial orientation of the fiber with respect to the local shear (see Fig. 2(*d*)) that in the Face-1 initial location the fiber is such that only basal slip is activated on the basal plane. The basal plane is initially perpendicular to the imposed shear direction. In such a situation, the lattice spin is twice as large as the rigid body spin. This has been shown in the Appendix of Beausir et al. [32]. However, even this very large initial rotation rate is not sufficient for the fiber to reach the ideal B fiber. The effect of DRX on the texture will be discussed below.

5.3.2 Texture in the Face-2 Position. In order to interpret the texture evolution in the Face-2 position, again an appropriate section of the ODF is examined, the $\varphi_2=30$ ° (see Fig. 14). Here the

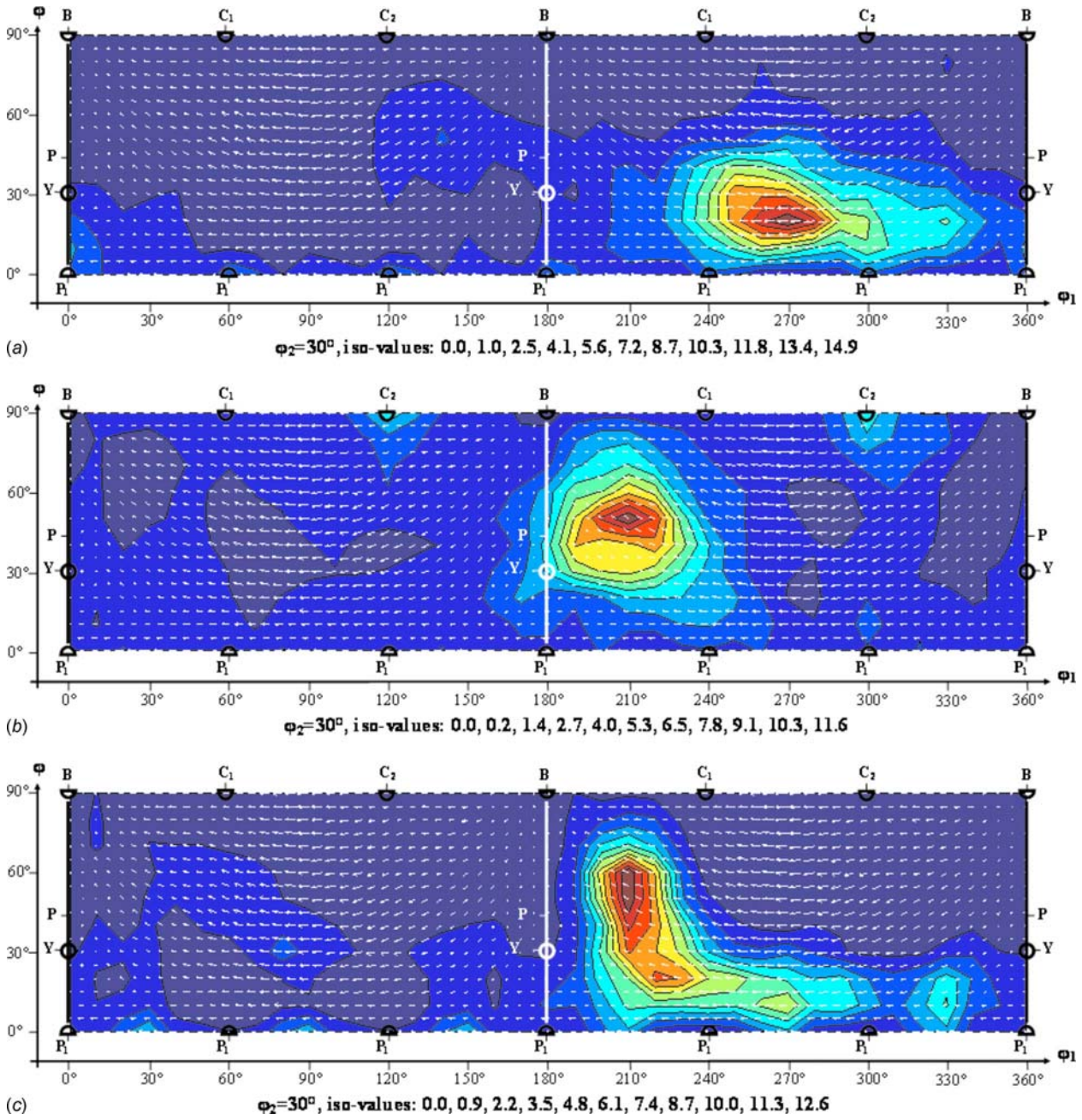

Fig. 14 Texture evolution for pure Mg in the ⟨⟨Face-2⟩⟩ position displayed in the $\varphi_2=30$ ° ODF section. (*a*) Initial texture, (*b*) deformation texture, and (*c*) simulation.

initial fiber crosses the section at the ($\varphi_1=270$ °, $\varphi=15$ °, $\varphi_2=30$ °) orientation. In all other $\varphi_2=$const sections, the fiber remains at the same position (it is a φ_2 fiber in contrast to the fiber in the AZ71 axisymmetric texture, which is a φ fiber). (Note that the maximum is not repeated with 180 ° periodicity in the φ_1 direction in orientation space as it would be usual for a simple shear texture—due to the sample symmetry—as there is no twofold symmetry of the texture around the *r* axis of the specimen for the present nonaxisymmetric initial texture.) After the $\gamma=1.3$ shear, the fiber moves toward the ideal P fiber (see Fig. 14(*b*)) approaching it by about 30 °. The superimposed predicted velocity field is in agreement with the observed rotation of the fiber. The predicted texture is very similar to the experimental one; the difference is that it shows a "tail" of the texture between the initial and final positions. However, the intensity along the tail is relatively low; actually, the maximum ODF position lies in another section, which will be presented in the DRX section below. Nevertheless, the ODF section presented in Fig. 14 was very useful for the interpretation of the texture development.

The interpretation of the texture development in the Ear-1 and Ear-2 positions can be done in a similar way as for the Face-1 and Face-2 textures; however, they are not detailed here in order to save space.

5.3.3 Hardening. Although the experimental torque–twist angle curves could not be converted into shear stress–shear strain curves for the pure Mg sample due to its nonaxisymmetric texture, during the texture development simulations, stress–strain curves were also obtained. They are plotted in Fig. 12(*b*) for the four local textures considered in the Mg sample. As can be seen, a

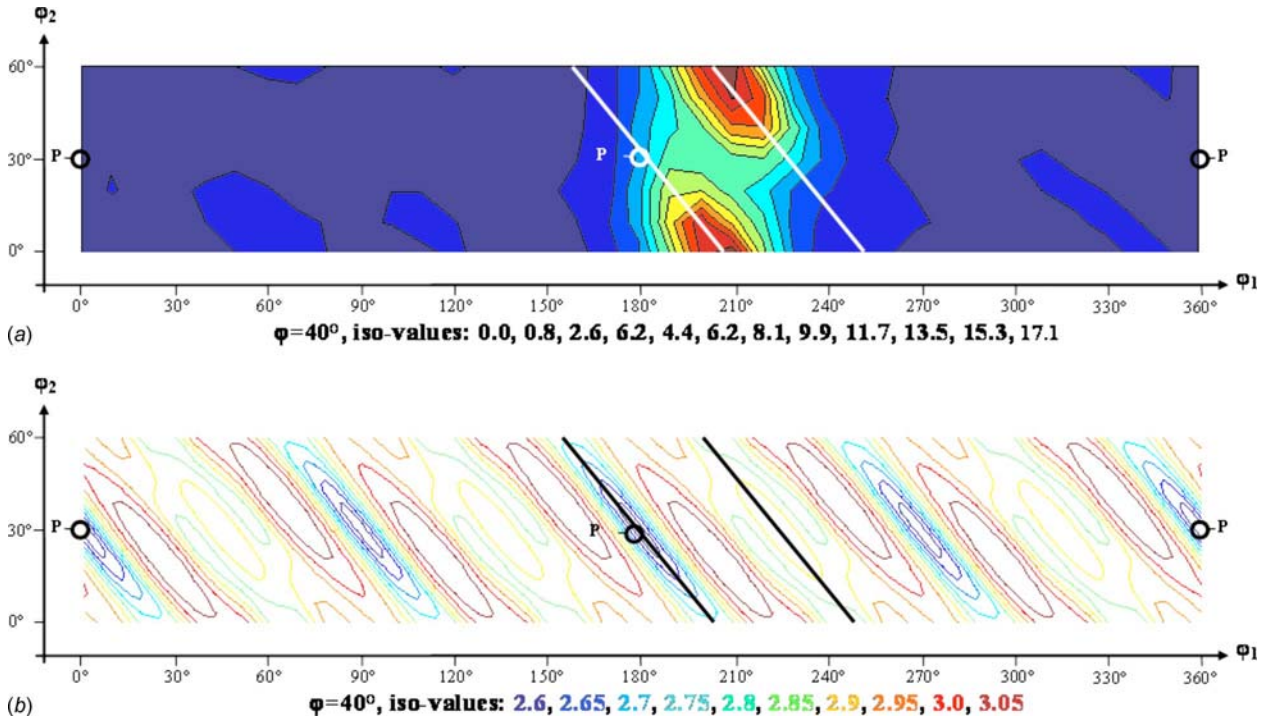

Fig. 15 (*a*) **Measured texture in the pure Mg sample in the ⟨⟨Face-2⟩⟩ position displayed in the $\varphi=40^\circ$ ODF section. (*b*) Map of the Taylor factor in the same section of the orientation space. Thick lines indicate the minimum Taylor factor position at the fiber position.**

small amount of softening was predicted for the Ear-1 and Face-2 textures, while significant strain hardening is obtained for the Ear-2 and Face-1 locations. As the slip system strengths were kept constant in the simulations, the observed behaviors can again be attributed to geometrical hardening effects that are due to the evolution of the texture.

5.3.4 Dynamic Recrystallization. The effect of DRX was neglected in the polycrystal simulations of the textures discussed above. This gives us the possibility to detect the differences in the textures that might be attributed to the occurrence of DRX. One commonly considered mechanism of DRX is the growth of nuclei that are rotated $\pm 30^\circ$ with respect to a "parent" grain [36–39]. In the present textures of pure Mg, the fibers are such that the common axis of rotation is the *c* axis of the crystals. Thus, when the mechanism of rotation by $\pm 30^\circ$ around axis c is operating, the newly formed grains will remain in the fiber. Consequently, the position of the fiber remains unchanged. Nevertheless, the intensity distribution along the fiber can be changed. This is exactly the case in the Face-1 texture shown in Fig. 13. The texture due to slip only retains the intensity distribution of the initial fiber (compare Figs. 13(*c*) and 13(*a*)), while in the recrystallization texture (Fig. 13(*b*)), the strength at the center of the fiber is increased.

Considering the above mentioned DRX mechanism by a rotation of $\pm 30^\circ$ of the newly formed grains, one can see that in such a mechanism when both the positive and negative rotations are applied with equal probability (no variant selection), the fiber intensity should tend to be uniform. The reason is that there are more orientations leaving the high intensity positions than those coming to the same position from low intensity places. The change in the experimental texture, however, is just the opposite as there is a strong peak in the middle of the fiber. Therefore, it is reasonable to assume that there is variant selection in such a DRX process.

The Taylor factor is frequently applied in DRX modeling, which can account for the stored energy differences in differently oriented grains, a driving force in the DRX process [40–42]. It is defined as follows:

$$M = \frac{\sum_s |\dot{\gamma}^s|}{\bar{\dot{\varepsilon}}} \tag{7}$$

Actually, the amount of slip is proportional to the Taylor factor, so the quantity of dislocations remaining in the crystal can be represented by *M*. The dislocation density is directly proportional to the stored energy. For the above reasons, the Taylor factor was calculated using the Taylor model. (Similar trends were obtained with the self-consistent model as well, with somewhat lower *M*-values.) The results are plotted in the same sections as the experimental ODF for the Face-1 and Face-2 textures in Figs. 13(*c*) and 15, respectively. As can be seen in both cases, the maximum intensity position of the ODF coincides with the local minimum of the Taylor factor. In Fig. 15, even the shape of the ODF follows the *M* factor variation. In conclusion, the Taylor factor seems to be a decisive factor in the development of the orientation density during DRX. It is, nevertheless, difficult to estimate at this point what the exact mechanism of the DRX process is. Namely, is it oriented nucleation and growth or perhaps selective growth? Both of them were identified in earlier DRX simulations [40,41]. However, these were carried out on copper. Further investigations are necessary to develop more precise ideas and possible modeling for the effect of DRX in the evolution of the ODF during large plastic strain of Mg.

5.3.5 Deformation Anisotropy. Finally, the formation of the ears and faces can be interpreted as follows: Due to the variations in the texture along the circumferential direction, the material anisotropy also varies as a function of the angular position. Consequently, when torsion loading is applied, the local response in the

strain of a material element is not exactly the same; it depends on its local anisotropy. As the initial anisotropy is determined by the initial fiber position, two directions will be the major axes of the anisotropy in a plane perpendicular to the bar axis: one parallel to the fiber axis and one perpendicular to it. The deformation behaviors at these two locations are very different. Most importantly, the Swift effect, which is very sensitive to the initial anisotropy, should be significantly different. The overall axial strain is shortening, however, with different amounts at these perpendicular directions. Then, by taking into account volume constancy, it follows that the stretching in the radial directions should be different, too. In this way, the initially circular cross section of the bar becomes distorted into regions that we refer to in this paper as ears and faces.

6 Conclusions

Two different Mg materials were examined in the present work by torsion testing. The main difference between them was their initial texture. For the AZ71 Mg material, the initial texture was a fiber parallel to the axis of the bar. For the pure Mg sample, the texture was not axisymmetric as the torsion sample was prepared from a rolled Mg plate. The texture development and the Swift effect were examined experimentally as well as by polycrystal simulations. From the results obtained, the following main conclusions can be obtained.

1. For both materials, the initial fiber texture was nearly maintained in a rotated position by a rotation mainly in the direction of the applied shear. The rotation was significantly larger than the rigid body rotation imposed in the test. This particularity was reproduced by the simulations as well. The initial textures were far from the ideal locations, which were not reached during the tests.
2. The experimental strain hardening was simulated successfully in AZ71 with polycrystal modeling without increasing the strength of the slip systems during deformation. Thus, the observed macroscopic hardening is a geometrical textural hardening.
3. In the pure Mg material, the sample changed its initial circular cross section into an elliptical one. This effect was due to the initial texture, which was not axisymmetric. Consequently, the deformation texture was also not axisymmetric. Local texture measurements carried out with EBSD together with polycrystal simulations permitted the interpretation of the texture development with the help of the rotation field characteristics of simple shear textures.
4. The local minimum values of the Taylor factor coincide with the maximum intensities of the ODF in the recrystallized fiber of the deformed pure Mg. It is proposed that the DRX process is controlled by the Taylor factor, which represents the stored energy in the crystal.

Acknowledgment

The authors thank Dr. Carlos Tomé (Los Alamos National Laboratory, USA) for the Swift-effect version of the VPSC code, José Luís Pérez Castellanos (Université Carlos III de Madrid, Spain) for providing the torsion test samples (AZ71), and Satyam Suwas (Indian Institute of Science, Bangalore) for the pure Mg samples. This work was partially funded by the Natural Sciences and Engineering Research Council of Canada (NSERC). K.W.N. is Canada Research Chair in Advanced Engineered Material Systems, and the support from this program is greatly appreciated.

References

[1] Sanchez, P., Pochenttino, A., Chauveau, T., and Bacroix, B., 2001, "Torsion Texture Development of Zirconium Alloys," J. Nucl. Mater., **298**, pp. 329–339.
[2] Evans, W. J., Jones, J. P., and Whittaker, M. T., 2005, "Texture Effects Under Tension and Torsion Loading Conditions in Titanium Alloys," Int. J. Fatigue, **27**, pp. 1244–1250.
[3] Swift, H. W., 1947, "Length Changes in Metals Under Torsional Overstrain," Engineering (London), **4**, pp. 253–257.
[4] Neale, K. W., and Schrivastava, S. C., 1985, "Finite Elastic-Plastic Torsion of a Circular Bar," Eng. Fract. Mech., **21**, pp. 747–754.
[5] Tóth, L. S., Jonas, J. J., Daniel, D., and Bailey, J. A., 1992, "Texture Development and Length Changes in Copper Bars Subjected to Free End Torsion," Textures Microstruct., **19**, pp. 245–262.
[6] Van Houtte, P., Aernoudlt, E., and Sekine, K., 1981, "Orientation Distribution Function Measurements of Copper and Brass Torsion Textures," *Proceedings ICOTOM 6*, ISIJ, Tokyo, Japan, S. Nagashima, ed., p. 337.
[7] Montheillet, F., Cohen, M., and Jonas, J. J., 1984, "Axial Stresses and Texture Development During the Torsion Testing of Al, Cu and α-Fe ," Acta Metall., **32**(11), pp. 2077–2089.
[8] Hughes, D. A., and Wenk, H. R., 1987, "The Effect of Stacking Fault Energy on the Texture on Nickel-Cobalt Solid Solutions at Large Strain," *Proceedings of ICOTOM 8*, Santa Fe, NM, Sept. 20–25, J. S. Kallend and G. Gottstein, eds., p. 455.
[9] Böhlke, T., Bertram, A., and Krempl, E., 2003, "Modeling of Deformation Induced Anisotropy in Free-End Torsion," Int. J. Plast., **19**, pp. 1867–1884.
[10] Duchêne, L., El Houdaigui, F., and Habraken, A. M., 2007, "Length Changes and Texture Prediction During Free End Torsion Test of Copper Bars With FEM and Remeshing Techniques," Int. J. Plast., **23**(8), pp. 1417–1438.
[11] Balasubramanian, S., and Anand, L., 2002, "Plasticity of Initially Textured Hexagonal Polycrystals at High Homologous Temperatures: Application to Titanium," Acta Mater., **50**, pp. 133–148.
[12] Barnett, M. R., 2001, "Influence of Deformation Condition and Texture on the High Temperature Flow Stress of Magnesium AZ31," J. Light Met., **1**, pp. 167–177.
[13] Fields, D. S., and Backofen, W. A., 1957, "Determination of Strain Hardening Characteristics by Torsion Testing," *Proceedings of ASTM*, 57, pp. 1259–1271.
[14] Qods, F., Tóth, L. S., and Van Houtte, P., 2005, "Modeling of Length Changes and Textures During Free End Torsion of Cylindrical Bars," Mater. Sci. Forum, **495–497**, pp. 1609–1614.
[15] Tóth, L. S., Qods, F., and Fundenberger, J. J., 2005, "Modeling of Axial Strain in Free-End Torsion of Textured Copper," Z. Metallkd., **96**, pp. 1038–1044.
[16] Yang, Q., and Ghosh, A. K., 2006, "Production of Ultrafine-Grain Microstructure in Mg Alloy by Alternate Biaxial Reverse Corrugation," Acta Mater., **54**, pp. 5147–5158.
[17] Beausir, B., Tóth, L. S., and Neale, K. W., 2007, "Ideal Orientations and Persistence Characteristics for h.c.p. Crystals in Simple Shear," Acta Mater., **55**, pp. 2695–2705.
[18] Nadai, A., 1950, *Theory of Flow and Fracture*, McGraw-Hill, New York, p. 349.
[19] Yang, Q., and Ghosh, A. K., 2006, "Deformation Behavior of Ultrafine-Grain (UFG) AZ31B Mg Alloy at Room Temperature," Acta Mater., **54**, pp. 5159–5170.
[20] Barnett, M. R., Keshavarz, Z., Beer, A. G., and Atwell, D., 2004, "Influence of Grain Size on the Compressive Deformation of Wrought Mg–3Al–1Zn," Acta Mater., **52**, pp. 5093–5103.
[21] Canova, G. R., Kocks, U. F., and Jonas, J. J., 1984, "Theory of Torsion Texture Development," Acta Metall., **32**, pp. 211–226.
[22] Lebensohn, R. A., and Tomé, C. N., 1993, "A Self-Consistent Anisotropic Approach for the Simulation of Plastic Deformation and Texture Development of Polycrystals—Application to Zirconium Alloys," Acta Metall., **41**, pp. 2611–2624.
[23] Agnew, S. R., Mehrotra, P., Lillo, T. M., Stoica, G. M., and Liaw, P. K., 2005, "Texture Evolution of Five Wrought Magnesium Alloys During Route A Equal Channel Angular Extrusion: Experiments and Simulations," Acta Mater., **53**, pp. 3135–3146.
[24] Staroselsky, A., and Anand, L., 2003, "A Constitutive Model for hcp Materials Deforming by Slip and Twinning: Application to Magnesium Alloy AZ31B," Int. J. Plast., **19**, pp. 1843–1864.
[25] Agnew, S. R., and Duygulu, O., 2005, "Plastic Anisotropy and the Role of Non-Basal Slip in Magnesium Alloy AZ31B," Int. J. Plast., **21**, pp. 1161–1193.
[26] Kim, W. J., Chung, S. W., Chung, C. S., and Kum, D., 2001, "Superplasticity in Thin Magnesium Alloy Sheets and Deformation Mechanism Maps for Magnesium Alloys at Elevated Temperatures," Acta Mater., **49**, pp. 3337–3345.
[27] Asaro, R. J., and Needleman, A., 1985, "Texture Development and Strain Hardening in Rate Dependent Polycrystals," Acta Metall., **33**, pp. 923–953.
[28] Neale, K. W., Tóth, L. S., and Jonas, J. J., 1990, "Large Strain Shear and Torsion of Rate-Sensitive fcc Polycrystals," Int. J. Plast., **6**, pp. 45–62.
[29] Van der Giessen, E., Wu, P. D., and Neale, K. W., 1992, "On the Effect of Plastic Spin on Large Strain Elastic-Plastic Torsion of Solid Bars," Int. J. Plast., **8**, pp. 773–801.
[30] Tóth, L. S., Gilormini, P., and Jonas, J. J., 1988, "Effect of Rate Sensitivity on the Stability of Torsion Textures," Acta Metall., **36**(12), pp. 3077–3091.
[31] Tóth, L. S., Jonas, J. J., and Neale, K. W., 1990, "Comparison of the Minimum Plastic Spin and Rate Sensitive Slip Theories for Loading of Symmetrical Crystal Orientations," Proc. R. Soc. London, Ser. A, **427**, pp. 201–219.
[32] Beausir, B., Suwas, S., Tóth, L. S., Neale, K. W., and Fundenberger, J. J., 2008, "Analysis of Texture Evolution in Magnesium During Equal Channel Angular Extrusion," Acta Mater., **56**(2), pp. 200–214.
[33] Beyerlein, I. J., Lebensohn, R. A., and Tomé, C. N., 2003, "Modeling Texture and Microstructural Evolution in the Equal Channel Angular Extrusion Process," Mater. Sci. Eng., A, **345**, pp. 122–138.
[34] Tomé, C. N., Tóth, L. S., and Skrotzki, W., 2007, "Swift Effect and Textures in

Free End Torsion of Ni–Al as Predicted From Self-Consistent Polycrystal Viscoplasticity," in preparation.
[35] Tóth, L. S., and Molinari, A., 1994, "Tuning a Self Consistent Viscoplastic Model by Finite Element Results, Part II: Application to Torsion Textures," Acta Metall., **42**, pp. 2459–2466.
[36] Galiyev, A., Kaibyshev, R., and Gottstein, G., 2001, "Correlation of Plastic Deformation and Dynamic Recrystallization in Magnesium Alloy ZK60," Acta Mater., **49**, pp. 1199–1207.
[37] Tan, J. C., and Tan, M. J., 2003, "Dynamic Continuous Recrystallization Characteristics in Two Stage Deformation of Mg–3Al–1Zn Alloy Sheet," Mater. Sci. Eng., A, **339**, pp. 124–132.
[38] Yi, S. B., Zaefferer, S., and Brokmeier, H. G., 2006, "Mechanical Behaviour and Microstructural Evolution of Magnesium Alloy AZ31 in Tension at Different Temperatures," Mater. Sci. Eng., A, **424**, pp. 275–281.
[39] Fatemi-Varzaneh, S. M., Zarei-Hanzaki, A., and Beladi, H., 2006, "Dynamic Recrystallization in AZ31 Magnesium Alloy," Mater. Sci. Eng., A, **456**(1–2), pp. 52–57.
[40] Tóth, L. S., and Jonas, J. J., 1992, "Modelling the Texture Changes Produced by Dynamic Recrystallization," Scr. Metall. Mater., **27**, pp. 359–363.
[41] Jonas, J. J., and Tóth, L. S., 1992, "Modelling Oriented Nucleation and Selective Growth During Dynamic Recrystallization," Scr. Metall. Mater., **27**, pp. 1575–1580.
[42] Mohamed, G., and Bacroix, B., 2000, "Role of Stored Energy in Static Recrystallization of Cold Rolled Copper Single and Multicrystals," Acta Mater., **48**, pp. 3295–3302.